

# Electron Doping Evolution of Magnetic Excitations and Spin-Orbit Excitons in $(\text{Sr}_{1-x}\text{La}_x)_3\text{Ir}_2\text{O}_7$

Xingye Lu,<sup>1,\*</sup> D. E. McNally,<sup>1</sup> M. Moretti Sala,<sup>2</sup> J. Terzic,<sup>3</sup> M. H. Upton,<sup>4</sup> D. Casa,<sup>4</sup> G. Cao,<sup>3</sup> and T. Schmitt<sup>1,†</sup>

<sup>1</sup>*Department of Synchrotron Radiation and Nanotechnology,  
Paul Scherrer Institut, CH-5232 Villigen PSI, Switzerland*

<sup>2</sup>*European Synchrotron Radiation Facility, BP 220, F-38043 Grenoble Cedex, France*

<sup>3</sup>*Department of Physics and Astronomy, University of Kentucky, Lexington, Kentucky 40506, USA*

<sup>4</sup>*Advanced Photon Source, Argonne National Laboratory, Argonne, Illinois 60439, USA*

(Dated: April 19, 2022)

We use resonant inelastic X-ray scattering at the Ir- $L_3$  edge to study the magnetic excitations and the spin-orbit excitons in the bilayer iridate  $(\text{Sr}_{1-x}\text{La}_x)_3\text{Ir}_2\text{O}_7$  ( $0 \leq x \leq 0.065$ ). With increasing doping  $x$ , the three-dimensional (3D) long range antiferromagnetic order (LAF) is gradually suppressed and evolves into a short range order (SAF) from  $x = 0$  to 0.05, followed by a transition from 3D SAF to 2D SAF between  $x = 0.05$  and 0.065. The  $x \leq 0.05$  samples exhibit doping-dependent damping and anisotropic softening in magnetic excitations and a large magnon gap. The metallic  $x = 0.065$  sample shows increased softening at  $(\frac{1}{4}, \frac{1}{4})$  but sizable hardening at  $(\frac{1}{2}, 0)$  with the magnon gap largely reduced. From the lack of  $c$ -axis magnetic correlations in  $x = 0.065$ , we conclude that electron doping suppresses the interlayer couplings and drives  $(\text{Sr}_{1-x}\text{La}_x)_3\text{Ir}_2\text{O}_7$  into a 2D SAF correlated metallic state hosting strong antiferromagnetic spin fluctuations. Meanwhile, the spin-orbit excitons at  $(\frac{1}{2}, 0)$  decrease in energy by 70 meV across the transition from 3D to 2D SAF, suggesting that magnetic correlations are crucial for stabilizing the Mott gap.

PACS numbers: 74.10.+v, 75.30.Ds, 78.70.Ck

The layered Ruddlesden-Popper iridate series  $\text{Sr}_{n+1}\text{Ir}_n\text{O}_{3n+1}$  ( $n = 1, 2$ ) that hosts novel  $J_{\text{eff}} = \frac{1}{2}$  Mott insulating states have recently attracted much interest because novel collective quantum states may be realized by doping these Mott insulators in the strong spin-orbit coupling (SOC) limit [1–5, 7, 8]. Distinct from 3d Mott insulators where strong on-site Coulomb electron correlation ( $U$ ) dominates [9], the  $J_{\text{eff}} = \frac{1}{2}$  Mott state in iridates is induced by cooperative interplay between crystal-field, SOC ( $\sim 0.4$  eV) and an intermediate  $U$  [4]. The strong SOC splits the  $t_{2g}(5d^5)$  band into two narrower bands, the  $j_{\text{eff}} = \frac{3}{2}$  quartet at lower energy and the  $j_{\text{eff}} = \frac{1}{2}$  doublet. The intermediate  $U$  in the half-filled  $j_{\text{eff}} = \frac{1}{2}$  band is therefore large enough to open a Mott insulating gap  $\Delta E$  [4]. The  $J_{\text{eff}} = \frac{1}{2}$  Mott state is usually accompanied by  $j_{\text{eff}} = \frac{1}{2}$  antiferromagnetic order (AFM), though the relationship between the AFM and  $\Delta E$  remains unclear [4, 6].

The single-layer  $\text{Sr}_2\text{IrO}_4$  is a benchmark of the  $J_{\text{eff}} = \frac{1}{2}$  state [3–5, 7] with a gap  $\Delta E \approx 0.6$  eV [10] and an in-plane canted AFM below the Neel temperature  $T_N = 240$  K [5, 11]. This pseudospin- $\frac{1}{2}$  AFM on a square lattice, as well as its spin dynamics, is similar to the spin- $\frac{1}{2}$  AFM in the superconducting parent compound  $\text{La}_2\text{CuO}_4$  [12–15]. Due to such similarities, it has been predicted that unconventional superconductivity might occur in doped  $\text{Sr}_2\text{IrO}_4$  [16, 17]. This has triggered substantial interest in exploring novel phases in doped  $\text{Sr}_2\text{IrO}_4$  and various exotic properties such as Fermi arcs and pseudogaps have been discovered in surface and bulk electron-doped  $\text{Sr}_2\text{IrO}_4$  [18–23]. It has been demonstrated that La doping introduces itinerant electrons, suppresses the three

dimensional (3D) long range AFM (LAF) in  $\text{Sr}_2\text{IrO}_4$  and drives  $\text{Sr}_{1-x}\text{La}_x\text{IrO}_4$  into a short range AFM (SAF) phase [19]. Moreover, resonant inelastic x-ray scattering (RIXS) measurements by Gretarsson *et al.* observed two dimensional (2D) SAF for  $x \geq 0.04$  and show that intense magnetic excitations persist up to  $x = 0.1$  [24]. The magnetic excitations in  $\text{Sr}_{1-x}\text{La}_x\text{IrO}_4$  show anisotropic softening and can be described by the pseudospin- $\frac{1}{2}$  model [24]. The doping evolution of the AFM and magnetic excitations is similar to that in hole doped cuprates [24, 25]. However, it seems difficult to induce a homogeneous metallic state up to La substitution limit in  $\text{Sr}_{1-x}\text{La}_x\text{IrO}_4$  [19, 23].

Compared with  $\text{Sr}_2\text{IrO}_4$ , bilayer  $\text{Sr}_3\text{Ir}_2\text{O}_7$  shows distinctively different magnetic order, spin dynamics and charge gap, though they share the same distorted  $\text{IrO}_2$  planes. Due to the interlayer couplings within bilayers,  $\text{Sr}_3\text{Ir}_2\text{O}_7$  exhibits a smaller gap  $\Delta E \approx 130$  meV [7, 27] and a  $c$ -axis  $G$ -type AFM ground state below  $T_N \approx 285$  K [8, 28]. RIXS studies revealed distinct magnons bearing a large magnon gap  $\approx 90$  meV [29, 30]. The small charge gap indicates that  $\text{Sr}_3\text{Ir}_2\text{O}_7$  lies close to a insulator-to-metal transition (IMT), and one could expect a homogeneous metallic state to develop by minor charge carrier doping. Indeed, an IMT and robust metallic state have been realized in  $(\text{Sr}_{1-x}\text{La}_x)_3\text{Ir}_2\text{O}_7$  for  $x \gtrsim 0.05$  [31, 32]. Since minor La dopants have little effect on  $\text{IrO}_2$  layers while driving the system across the IMT,  $(\text{Sr}_{1-x}\text{La}_x)_3\text{Ir}_2\text{O}_7$  provides an ideal platform to exploring novel phenomena arising from charge carrier doped  $J_{\text{eff}} = \frac{1}{2}$  Mott states, in the presence of strong interlayer coupling [29, 30]. However, the doping evolution of the

ground state of  $(\text{Sr}_{1-x}\text{La}_x)_3\text{Ir}_2\text{O}_7$  is still under intense debate [32–35]. Angle-resolved photoemission (ARPES) measurements revealed a strong coherent quasiparticle peak and suggested a weakly correlated Fermi liquid ground state in  $(\text{Sr}_{0.95}\text{La}_{0.05})_3\text{Ir}_2\text{O}_7$  [33]. In contrast, a doping-dependent negative electronic compressibility was discovered in later ARPES measurements, indicating an exotic correlated metallic state [35]. Correlations in the metallic state were also suggested by transport, structural and neutron scattering measurements [32]. In order to reveal the nature of the metallic state, a detailed study of the elementary excitations is required that can determine the doping evolution of the electronic interactions, especially the magnetic couplings. Furthermore, it will be interesting to study the doping evolution of the strong interlayer coupling in doped  $\text{Sr}_3\text{Ir}_2\text{O}_7$ , which is crucial for the  $c$ -axis  $G$ -type AFM [8] and the large magnon gap in  $\text{Sr}_3\text{Ir}_2\text{O}_7$  [29, 30].

Here, we present measurements of the doping dependence of the magnetic order and the elementary excitations across the electron-doping driven IMT in  $(\text{Sr}_{1-x}\text{La}_x)_3\text{Ir}_2\text{O}_7$  ( $x = 0, 0.02, 0.03, 0.05$  and  $0.065$ ) using Ir  $L_3$  edge RIXS. Our results reveal an evolution of the AFM from 3D LAF to 3D SAF ( $0.02 < x \leq 0.05$ ) and subsequent 2D SAF deep in the metallic state ( $x = 0.065$ ). We present a detailed analysis of the doping-dependent magnetic excitations and spin-orbit excitons, from which the doping evolution of the magnetic couplings and the nature of the metallic state are determined.

The  $(\text{Sr}_{1-x}\text{La}_x)_3\text{Ir}_2\text{O}_7$  single crystals were grown by the flux method, as described elsewhere [26, 31]. The average La concentration  $x$  were determined by energy-dispersive X-ray analysis. RIXS measurements of  $(\text{Sr}_{1-x}\text{La}_x)_3\text{Ir}_2\text{O}_7$  were carried out at the ID20 beamline ( $x = 0.02, 0.05$  and  $0.065$ ) of the European Synchrotron Radiation Facility (ESRF) and the 27ID-B beamline ( $x = 0$  and  $0.03$ ) at the Advanced Photon Source (APS) [37, 38]. By using a Rowland spectrometer equipped with spherical diced Si(844) analyzer ( $R = 2\text{m}$ ), overall energy resolutions about 25 meV and 30 meV are achieved at ID20 and 27ID-B, respectively. The scattering plane is set within the horizontal plane, as well as the incident photon polarization ( $\pi$  polarization). To facilitate comparison with previous results [8, 30], we use tetragonal notation in presenting our RIXS results and define the momentum transfer  $\mathbf{Q}$  in reciprocal space as  $\mathbf{Q} = H\mathbf{a}^* + K\mathbf{b}^* + L\mathbf{c}^*$ , where  $H$ ,  $K$ , and  $L$  are Miller indices and  $\mathbf{a}^* = \hat{\mathbf{a}}\frac{2\pi}{a}$ ,  $\mathbf{b}^* = \hat{\mathbf{b}}\frac{2\pi}{b}$ ,  $\mathbf{c}^* = \hat{\mathbf{c}}\frac{2\pi}{c}$  with  $a \approx b \approx 3.9 \text{ \AA}$ , and  $c = 20.9 \text{ \AA}$  for  $\text{Sr}_3\text{Ir}_2\text{O}_7$ . In this notation, the wave vector of the  $c$ -axis  $G$ -type AFM is  $\mathbf{q} = (\frac{1}{2}, \frac{1}{2}, 0)$  [29, 30].

We first describe the doping evolution of the magnetic order. Figure 1(a) is a schematic magnetic and electronic phase diagram of  $(\text{Sr}_{1-x}\text{La}_x)_3\text{Ir}_2\text{O}_7$ , drawn according to previous works [31, 32]. The doping levels  $x$  measured

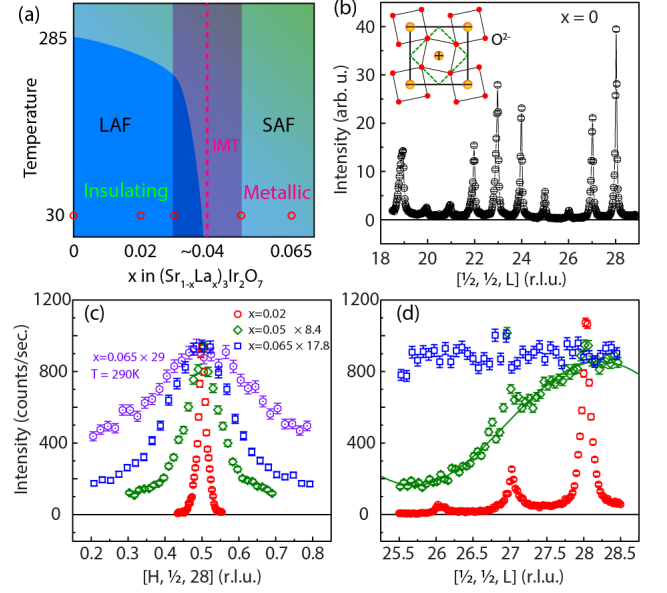


FIG. 1. (color online). (a) Schematic electronic phase diagram of  $(\text{Sr}_{1-x}\text{La}_x)_3\text{Ir}_2\text{O}_7$ , adapted from ref. [31, 32]. LAF and SAF are long range and short range antiferromagnetic order, respectively. IMT is insulator-to-metal transition, which occurs at  $x \sim 0.04$ . The dopings used in present study are marked by red circles. (b)  $L$  scan of the  $c$ -axis  $G$ -type anti-ferromagnetic order for  $x = 0$ . (inset) In-plane spin arrangement of  $\text{Ir}^{4+}$ , where the  $\text{IrO}_6$  octahedra are rotated by  $\sim 11^\circ$  around  $c$  axis. The black solid square and green dashed square mark the orthorhombic and tetragonal unit cells, respectively. (c),(d) Doping dependent  $H$  and  $L$  scans across the magnetic Bragg peak  $(\frac{1}{2}, \frac{1}{2}, 28)$ . All the measurements were performed at 30 K unless otherwise indicated.

at  $T = 30 \text{ K}$  are indicated by red circles. To characterize the doping dependent AFM, we have measured the magnetic Bragg peaks along  $[H, \frac{1}{2}, 28]$  and  $[\frac{1}{2}, \frac{1}{2}, L]$  for  $x = 0, 0.02, 0.05$ , and  $0.065$  using the elastic channel of the RIXS spectrometer. The  $L$  scan for  $x = 0$  displays magnetic Bragg peaks from  $L = 19$  to  $28$  with an intensity modulation, which has a period controlled by the ratio between lattice parameter  $c$  and bilayer distance  $(\frac{c}{d} \approx 5.1)$ , in agreement with previous reports [8]. Upon electron doping, the 3D LAF persists for  $x = 0.02$  but becomes short ranged for  $x = 0.05$ , as indicated by the broad peaks along both  $H$  and  $L$  in Figs. 1(c) and 1(d). The  $L$  scan for the metallic  $x = 0.05$  sample deserves special attention. It reveals a broad feature superimposed on a flat background, and is well fitted by a sum of the bilayer antiferromagnetic structural factor  $\cos^2(\frac{2\pi d}{c})$  [8] and a constant background [green solid curve in Fig. 1(d)]. The presence of this broad feature indicates that the magnetic correlation length along  $c$  axis has decreased to a very small value comparable with the bilayer distance. This hints that the  $c$ -axis magnetic correlations supporting the  $G$ -type AFM are on the verge of disappearing, although the interlayer coupling is still

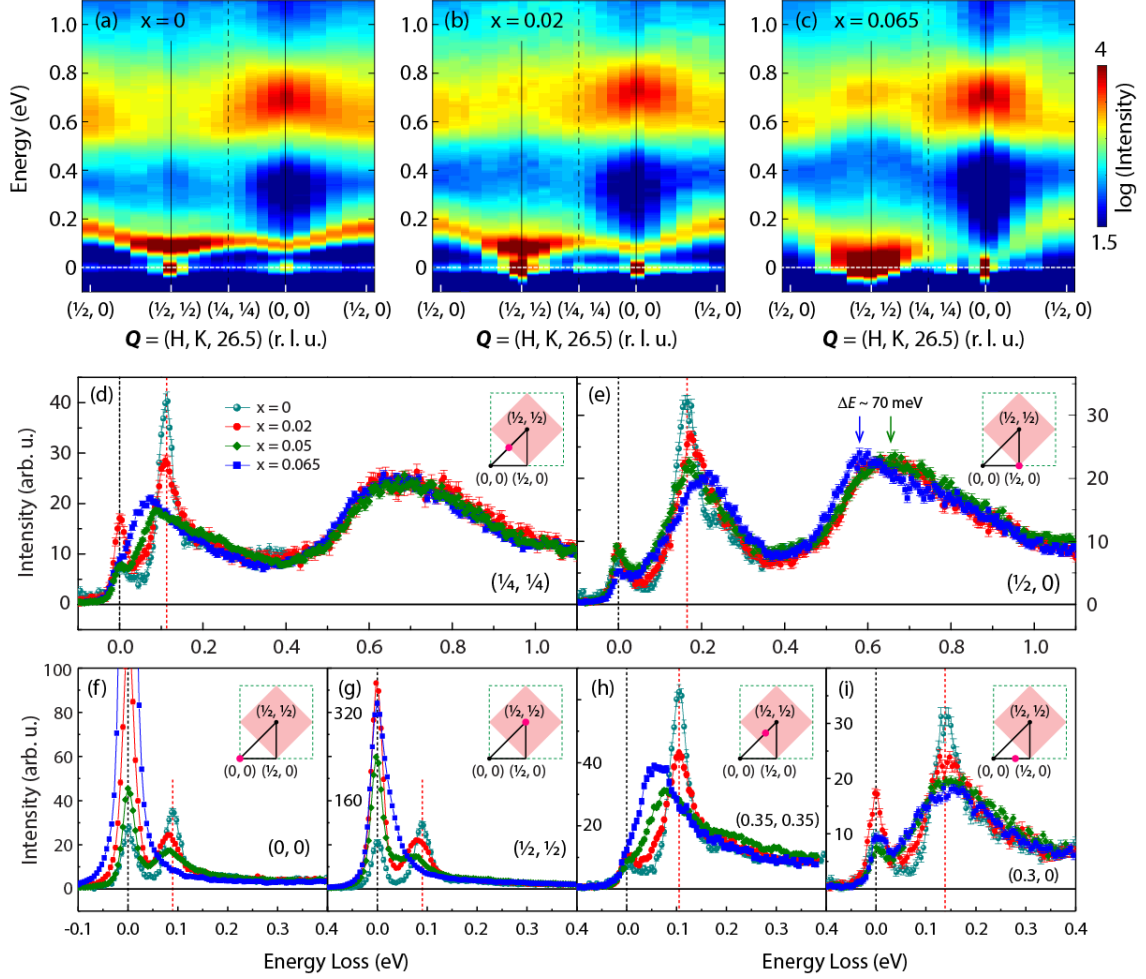


FIG. 2. (color online). (a)-(c) In-plane momentum dependence of RIXS spectra of  $(\text{Sr}_{1-x}\text{La}_x)_3\text{Ir}_2\text{O}_7$  for  $x = 0$ ,  $x = 0.02$  and  $0.065$ . (d)-(e) Comparison of the magnetic excitations and spin-orbit excitons between  $x = 0, 0.02, 0.05$  and  $0.065$  collected at  $\mathbf{Q} = (\frac{1}{4}, \frac{1}{4})$  and  $(\frac{1}{2}, 0)$ . (f)-(i) Doping dependence of the magnetic excitations at  $\mathbf{Q} = (0, 0)$ ,  $(\frac{1}{2}, \frac{1}{2})$ ,  $(0.35, 0.35)$  and  $(0.3, 0)$ . The insets in (d)-(i) illustrate the reciprocal space where the green dashed square and the pink solid square are the tetragonal Brillouin zone and the AFM Brillouin zone, respectively. The pink filled circles mark the vector positions for (d)-(i). The vertical red dashed lines mark the peak position of the magnetic excitations of the  $x = 0$  sample. The blue and green arrows in (e) show the peak positions of the spin-orbit excitons and  $\Delta E$  marks the energy difference of the peak positions.

present. The constant background can be attributed to a vanishing of the 3D SAF in a partial volume of the sample. This is in agreement with the percolative nature of the IMT, assuming that charge carriers are suppressing the magnetic order [29]. For  $x = 0.065$ , the  $L$  scan becomes featureless while the broader in-plane magnetic Bragg peak remains and persists at 290K [Fig.1(c) and 1(d)]. This indicates that further doping destroys the interlayer couplings that support the 3D SAF and drives the system into a robust 2D SAF state. This corroborates our explanation of the  $L$  scan for  $x = 0.05$ .

To further understand the doping-dependent electronic interactions across the IMT and the transitions between 3D LAF and 2D SAF, we have measured the magnetic excitations and the spin-orbit excitons on  $x = 0, 0.02, 0.03, 0.05$  and  $0.065$  [Figs. 2 and 3]. The in-plane

momentum dependent RIXS for  $x = 0, 0.02$  and  $0.065$  are shown as color maps in Figs. 2(a)-(c). For  $x = 0$ , the overall dispersion, the large spin-wave energy gap and the spectral-weight distribution are consistent with a previous report measured at the same  $L$  [29]. In addition, our results on  $(\text{Sr}_{1-x}\text{La}_x)_3\text{Ir}_2\text{O}_7$  reveal clear dispersive spin-orbit excitons exhibiting similar energy scale and dispersion with that in  $\text{Sr}_2\text{IrO}_4$ , in line with previous reports [7, 12, 13, 41, 42]. With increasing La concentration, the magnetic excitations are damped: they broaden in energy and decrease in intensity. This damping has been reported in other charge-carrier doped 2D correlated systems such as cuprates and iron pnictides [43–47].

The intensity and dispersion of the magnetic excitations exhibit a strong doping dependence [Figs. 2 and 3]. The dispersions are symmetric about  $(\frac{1}{4}, \frac{1}{4})$  and change

less from  $x = 0$  to  $x = 0.03$  [Fig. 3(a)]. They follow the fitting of the bilayer model as described by Kim *et al.* [Fig. 3] [29]. Across the IMT to  $x = 0.05$ , the dispersion becomes asymmetric with a different gap size at  $(\frac{1}{2}, \frac{1}{2})$  and  $(0, 0)$ . A substantial softening occurs along  $(\frac{1}{2}, \frac{1}{2})$ - $(\frac{1}{4}, \frac{1}{4})$  while the band top at  $(\frac{1}{2}, 0)$  remains unchanged [Figs. 2 and 3(b)]. This anisotropic softening is followed by a further softening at  $(\frac{1}{4}, \frac{1}{4})$  and, surprisingly, a sizable hardening at  $(\frac{1}{2}, 0)$  in  $x = 0.065$  [Figs. 2 and 3]. Furthermore, the large magnon gap in  $x \leq 0.05$  collapses dramatically in  $x = 0.065$  [Figs. 2(f), 2(g) and 3(b)], where the magnetic excitations at  $(\frac{1}{2}, \frac{1}{2})$  overlap with the elastic magnetic scattering [Fig. 2(g)], whereas a weak signal is observed at  $(0, 0)$  [Fig. 2(f)] [39]. A similar anisotropic softening between  $(\frac{1}{4}, \frac{1}{4})$  and  $(\frac{1}{2}, 0)$  was observed in  $\text{Sr}_{2-x}\text{La}_x\text{IrO}_4$  and attributed to the interaction between magnetic moments and emergent itinerant electrons having developed a Fermi surface at  $(\frac{1}{4}, \frac{1}{4})$  [23, 25]. The same explanation can be applied here since La introduces itinerant electrons and Fermi pockets have been well developed at  $(\frac{1}{4}, \frac{1}{4})$  in metallic  $(\text{Sr}_{1-x}\text{La}_x)_3\text{Ir}_2\text{O}_7$  [33–35]. Therefore the anisotropic softening is in line with that in  $\text{Sr}_{2-x}\text{La}_x\text{IrO}_4$ , indicative of a similar role of the emergent itinerant electrons.

The hardening of the magnetic excitations at  $(\frac{1}{2}, 0)$  and the collapse of the magnetic gap occur between  $x = 0.05$  and  $0.065$  where the system evolves from 3D SAF to 2D SAF. Since the AFM along  $c$ -axis is absent in 2D SAF, we expect that the bilayer couplings will be greatly suppressed in  $x = 0.065$ . It is then natural to attribute the dramatic change in dispersion to the suppression of the bilayer couplings. In the absence of  $c$ -axis magnetic correlations,  $(\text{Sr}_{1-x}\text{La}_x)_3\text{Ir}_2\text{O}_7$  is akin to the single-layer  $\text{Sr}_{2-x}\text{La}_x\text{IrO}_4$  ( $x \geq 0.04$ ), in which the magnetic excitations are gapless and have a larger band top at  $(\frac{1}{2}, 0)$  [24]. Indeed, we find the 2D pseudospin- $\frac{1}{2}$  ( $J - J_2 - J_3$ ) model used for  $\text{Sr}_2\text{IrO}_4$  captures the overall dispersion and generates similar fitted parameters as  $\text{Sr}_{2-x}\text{La}_x\text{IrO}_4$  ( $x \geq 0.04$ ) [Table I and Fig. 3], indicating that doped itinerant electrons drive  $\text{Sr}_3\text{Ir}_2\text{O}_7$  into a 2D magnetic system exhibiting strong antiferromagnetic spin fluctuations [24]. The strong magnetic excitations in  $x = 0.065$  demonstrates that metallic  $(\text{Sr}_{1-x}\text{La}_x)_3\text{Ir}_2\text{O}_7$  hosts strong electron correlations like its parent compound, and in agreement with a correlated metallic picture [32].

We have fitted the dispersions by the bilayer model to obtain the magnetic couplings as described in detail in ref. [29] [Table I and Fig. 3] [39]. In this model,  $c$ -axis couplings  $J_c$  and  $J_{2c}$  and out-of-plane Dzyaloshinsky-Moriya (DM) interaction  $D_c$  are responsible for the bilayer splitting of the acoustic and optical branches, and the spin gap arises from the anisotropic couplings  $\Gamma$  (intra-layer) and  $\Gamma_c$  (inter-layer) [29]. By adjusting  $J$ ,  $J_2$ ,  $J_3$  and  $J_c$ , our fitting results of the  $x = 0$  dispersion is consistent with a previous report [Table I] [29]. Due to the presence of interlayer couplings, our fitting for  $x \leq 0.05$

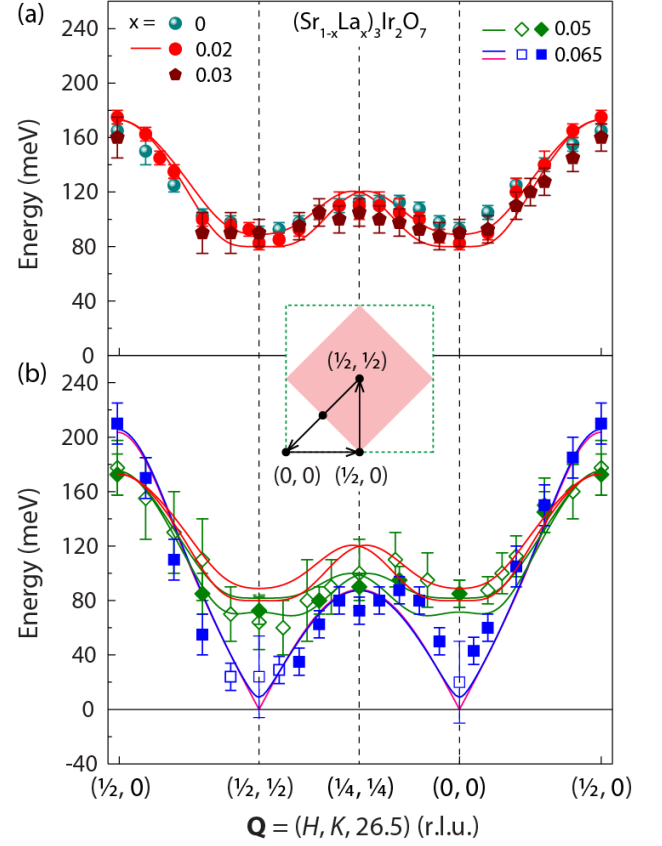


FIG. 3. (color online). Doping dependent dispersions of magnetic excitations for  $(\text{Sr}_{1-x}\text{La}_x)_3\text{Ir}_2\text{O}_7$  ( $x = 0, 0.02, 0.03, 0.05$  and  $0.065$ ). The dispersions for  $x \leq 0.05$  and the blue solid squares of  $x = 0.065$  are obtained by picking the peak positions of the magnetic excitations. The blue open squares of  $x = 0.065$  are fitting results of the magnetic excitations close to  $(\frac{1}{2}, \frac{1}{2})$  and  $(0, 0)$ . Open and filled green diamonds correspond to measurements of the same crystal at different beamtimes. The red, green and blue curves fits the dispersions for  $x = 0.02, 0.05$  and  $0.065$  using bilayer model [29], respectively. The pink curve is a fitting of the dispersion for  $0.065$  according to the  $J - J_2 - J_3$  model used to fit doped  $\text{Sr}_2\text{IrO}_4$  [24].

has been performed by adjusting only  $J$ ,  $J_2$  and  $J_3$ . For  $x = 0.065$ , we fit all the parameters to account for the suppression of the interlayer couplings [Table I [39]]. As shown in Fig. 3, our fitting successfully describes the anisotropic softening and collapse of the magnon gap. With increasing doping,  $J$  is suppressed monotonically while  $J_2$  decreases and changes sign across  $x = 0.05$ , followed by an enhancement in magnitude in  $x = 0.065$ . The anisotropic couplings ( $\Gamma$  and  $\Gamma_c$ ) are suppressed since the magnon gap collapses.  $J_c$ ,  $J_{2c}$  and  $D_c$  vanish because the bilayer splitting of the two branches disappear in 2D SAF state.

Though the bilayer model and  $J - J_2 - J_3$  model roughly describe the anisotropic softening and gap collapse, they fail to capture the asymmetry of the dis-

perturbations for metallic  $x = 0.05$  and  $0.065$  since these two models are intrinsically symmetric about  $(\frac{1}{4}, \frac{1}{4})$ . As shown in Fig. 3(b), the dispersion (data points) lie below the fitted line along the high symmetry directions  $(\frac{1}{2}, 0)$ - $(\frac{1}{2}, \frac{1}{2})$ - $(\frac{1}{4}, \frac{1}{4})$  but above the fitting along  $(\frac{1}{4}, \frac{1}{4})$ - $(0, 0)$ - $(\frac{1}{2}, 0)$ . This was also observed in  $\text{Sr}_{2-x}\text{La}_x\text{IrO}_4$  [24, 25] and could be attributed to different damping rates near  $(\frac{1}{2}, \frac{1}{2})$  and  $(0, 0)$ , but the underlying origin is still unclear [48].

TABLE I. Doping-dependent exchange couplings  $J$ ,  $J_2$ ,  $J_3$  and  $J_c$  obtained by fitting according to the bilayer model reported in Ref. [29] (row 1-5) (in units of meV). The  $J_c$  for  $x = 0.02$  and  $0.05$  are fixed at 27.4 meV. The 6th row is the best fitting of  $x = 0.065$  according to the  $J - J_2 - J_3$  model used for  $\text{Sr}_2\text{IrO}_4$ .

x	$J$	$J_2$	$J_3$	$J_c$
0	93	11.9	14.6	25.2 [29]
0	95.8	13.6	15.8	27.4
0.02	86.6	6.3	16.3	$\equiv 27.4$
0.05	74.7	-0.2	18.8	$\equiv 27.4$
0.065	53	-24	17.6	0.5
0.065	43.8	-29	14.4	-

We now discuss the doping-dependence of the spin-orbit excitons observed in our RIXS measurements [Figs. 2(d) and 2(e)]. A sudden decrease of the spin-orbit exciton energy ( $\Delta E \sim 70\text{meV}$ ) at  $(\frac{1}{2}, 0)$  occurs between  $x = 0.05$  and  $0.065$ . This decrease of the spin-orbit exciton energy at  $(\frac{1}{2}, 0)$  is coincident in momentum and fall into the similar doping range ( $0.04 \leq x \leq 0.057$ ) with the sudden reduction of the indirect Mott gap observed by ARPES [35]. We showed in Figs 1 and 2 that AFM along the  $c$ -axis disappears and magnetic couplings are modified across the 3D SAF to 2D SAF transition between  $x = 0.05$  and  $0.065$ . Therefore, we suggest that the altered magnetic correlations result in a decrease of the spin-orbit-exciton energy and the indirect Mott gap at  $(\frac{1}{2}, 0)$  and that magnetic correlations play an important role in creating and stabilizing the Mott gap. However, how to quantitatively reconcile the small doping dependence of the dispersive spin-orbit excitons with the evolution of the electronic structure remain elusive, as the spin-orbit excitons measured by RIXS are bosonic excitations connecting occupied  $j_{\text{eff}} = \frac{3}{2}$  and *unoccupied* states of  $j_{\text{eff}} = \frac{1}{2}$  while ARPES measures fermionic quasielectrons of occupied states [40].

In summary, our RIXS measurements on  $(\text{Sr}_{1-x}\text{La}_x)_3\text{Ir}_2\text{O}_7$  unveil an evolution of the AFM from 3D LAF to 3D SAF and subsequent 2D SAF deep in the metallic state [Fig. 1]. Following this, we show that the gapped spin waves undergo an anisotropic damping with increasing doping and largely suppressed magnetic gap in the 2D SAF metallic regime [Figs. 2 and 3]. This indicates that the doped itinerant electrons

suppress the AFM by weakening the magnetic couplings and drive the system into a 2D SAF correlated metallic state hosting strong AFM spin fluctuations. Meanwhile, a dramatic energy decrease of the spin-orbit excitons at  $(\frac{1}{2}, 0)$  across the 3D-to-2D SAF transition suggests that magnetic correlations are crucial for creating the Mott gap. Our results provide a solid experimental basis that will guide future theoretical works on the physics of doping the SOC-induced Mott insulators in the presence of strong interlayer coupling. In addition, the correlated metallic state hosting strong AFM spin fluctuations of  $j_{\text{eff}} = \frac{1}{2}$  in  $(\text{Sr}_{1-x}\text{La}_x)_3\text{Ir}_2\text{O}_7$  could be a new platform for realizing novel quantum phases by applying internal or external perturbations.

## ACKNOWLEDGEMENTS

We thank Matteo Rossi (ESRF) for helpful discussions. The work in Paul Scherrer Institut is supported by the Swiss National Science Foundation through its Sinergia network Mott Physics Beyond the Heisenberg (MPBH) Model and NCCR-MARVEL. Xingye Lu acknowledges financial support from the European Community's Seventh Framework Program (FP7/2007-2013) under grant agreement NO. 290605 (COFUND: PSI-FELLOW). The work at the University of Kentucky was supported by NSF through Grant No. DMR-1265162 and by the Department of Energy (BES) through Grant No. DE-FG02-98ER45707 (P.S.).

\* xingye.lu@psi.ch

† thorsten.schmitt@psi.ch

- [1] W. Witczak-Krempa, G. Chen, Y. B. Kim, and L. Balents, *Annu. Rev. Condens. Matter Phys.* **5**, 57 (2014).
- [2] D. Pesin and L. Balents, *Nature Physics* **6**, 376 (2010).
- [3] Jeffrey G. Rau, Eric Kin-Ho Lee, and Hae-Young Kee, *Annu. Rev. Condens. Matter Phys.* **7**, 195 (2015).
- [4] B. J. Kim, Hosub Jin, S. J. Moon, J.-Y. Kim, B.-G. Park, C. S. Leem, Jaehun Yu, T. W. Noh, C. Kim, S.-J. Oh, J.-H. Park, V. Durairaj, G. Cao, and E. Rotenberg, *Phys. Rev. Lett.* **101**, 076402 (2008).
- [5] B. J. Kim, H. Ohsumi, T. Komesu, S. Sakai, T. Morita, H. Takagi, and T. Arima, *Science* **323**, 1329 (2009).
- [6] R. Arita, J. Kunes, A. V. Kozhevnikov, A. G. Eguiluz, and M. Imada, *Phys. Rev. Lett.* **108**, 086403 (2012).
- [7] S. J. Moon, H. Jin, K. W. Kim, W. S. Choi, Y. S. Lee, J. Yu, G. Cao, A. Sumi, H. Funakubo, C. Bernhard, and T. W. Noh, *Phys. Rev. Lett.* **101**, 226402 (2008).
- [8] J. W. Kim, Y. Choi, Jungho Kim, J. F. Mitchell, G. Jackeli, M. Daghofer, J. van den Brink, G. Khaliullin, and B. J. Kim, *Phys. Rev. Lett.* **109**, 037204 (2012).
- [9] Patrick A. Lee, Naoto Nagaosa, Xiao-Gang Wen, *Rev. Mod. Phys.* **78**, 17 (2006).
- [10] J. Nichols, N. Bray-Ali, A. Ansary, G. Cao, and Kwok-Wai Ng, *Phys. Rev. B* **89**, 085125 (2014).



- [11] F. Ye, S. Chi, B. C. Chakoumakos, J. A. Fernandez-Baca, T. Qi, and G. Cao, *Phys. Rev. B* **87**, 140406 (2013).
- [12] Jung-ho Kim, D. Casa, M. H. Upton, T. Gog, Young-June Kim, J. F. Mitchell, M. van Veenendaal, M. Daghofer, J. van den Brink, G. Khaliullin, and B. J. Kim, *Phys. Rev. Lett.* **108**, 177003 (2012).
- [13] Jung-ho Kim, M. Daghofer, A. H. Said, T. Gog, J. van den Brink, G. Khaliullin and B. J. Kim, *Nature Communications* **5**, 4453 (2014).
- [14] R. Coldea et al., *Phys. Rev. Lett.* **86**, 5377 (2001).
- [15] N. S. Headings, S. M. Hayden, R. Coldea, and T. G. Perring, *Phys. Rev. Lett.* **105**, 247001 (2010).
- [16] Fa Wang and T. Senthil, *Phys. Rev. Lett.* **106**, 136402 (2011).
- [17] Hiroshi Watanabe, Tomonori Shirakawa, and Seiji Yunoki, *Phys. Rev. Lett.* **110**, 027002 (2013).
- [18] M. Ge, T. F. Qi, O. B. Korneta, D. E. De Long, P. Schlottmann, W. P. Crummett, and G. Cao, *Phys. Rev. B* **84**, 100402(R) (2011).
- [19] Xiang Chen, Tom Hogan, D. Walkup, Wenwen Zhou, M. Pokharel, Mengliang Yao, Wei Tian, Thomas Z. Ward, Y. Zhao, D. Parshall, C. Opeil, J. W. Lynn, Vidya Madhavan, and Stephen D. Wilson, *Phys. Rev. B* **92**, 075125 (2015).
- [20] Y. K. Kim, O. Krupin, J. D. Denlinger, A. Bostwick, E. Rotenberg, Q. Zhao, J. F. Mitchell, J. W. Allen, B. J. Kim, *Science* **345**, 187 (2014).
- [21] Y. J. Yan, M. Q. Ren, H. C. Xu, B. P. Xie, R. Tao, H. Y. Choi, N. Lee, Y. J. Choi, T. Zhang, and D. L. Feng, *Phys. Rev. X* **5**, 041018 (2015).
- [22] Y. K. Kim, N. H. Sung, J. D. Denlinger, and B. J. Kim, *Nat. Phys.* **12**, 37 (2016).
- [23] A. de la Torre, S. McKeown Walker, F. Y. Bruno, S. Ricc , Z. Wang, I. Gutierrez Lezama, G. Scheerer, G. Giriat, D. Jaccard, C. Berthod, T. K. Kim, M. Hoesch, E. C. Hunter, R. S. Perry, A. Tamai, and F. Baumberger, *Phys. Rev. Lett.* **115**, 176402 (2015).
- [24] H. Gretarsson, N. H. Sung, J. Porras, J. Bertinshaw, C. Dietl, Jan A. N. Bruin, A. F. Bangura, R. Dinnebier, Jung-ho Kim, A. Al-Zein, M. Moretti Sala, M. Krisch, M. Le Tacon, B. Keimer, B. J. Kim, arXiv:1603.07547 (2016).
- [25] X. Liu, M. P. M. Dean, Z. Y. Meng, M. H. Upton, T. Qi, T. Gog, Y. Cao, J. Q. Lin, D. Meyers, H. Ding, G. Cao, and J. P. Hill, arXiv:1601.02172 (2016).
- [26] G. Cao, Y. Xin, C. S. Alexander, J. E. Crow, P. Schlottmann, M. K. Crawford, R. L. Harlow, and W. Marshall, *Phys. Rev. B* **66**, 244412 (2002).
- [27] Y. Okada, D. Walkup, H. Lin, C. Dhital, T.-R. Chang, S. Khadka, W. Zhou, H.-T. Jeng, M. Paranjape, A. Bansil, Z. Wang, S. D. Wilson, and V. Madhavan, *Nat. Mater.* **12**, 707 (2013).
- [28] S. Boseggia, R. Springell, H. C. Walker, A. T. Boothroyd, D. Prabhakaran, D. Wermeille, L. Bouchenoire, S. P. Collins, and D. F. McMorrow, *Phys. Rev. B* **85**, 184432 (2012).
- [29] Jung-ho Kim, A. H. Said, D. Casa, M. H. Upton, T. Gog, M. Daghofer, G. Jackeli, J. van den Brink, G. Khaliullin, and B. J. Kim, *Phys. Rev. Lett.* **109**, 157402 (2012).
- [30] M. Moretti Sala, V. Schnells, S. Boseggia, L. Simonelli, A. Al-Zein, J. G. Vle, L. Paolasini, E. C. Hunter, R. S. Perry, D. Prabhakaran, A. T. Boothroyd, M. Krisch, G. Monaco, H. M. Ronnow, D. F. McMorrow, and F. Mila, *Phys. Rev. B* **92**, 024405 (2015).
- [31] L. Li, P. P. Kong, T. F. Qi, C. Q. Jin, S. J. Yuan, L. E. DeLong, P. Schlottmann, and G. Cao, *Phys. Rev. B* **87**, 235127 (2013).
- [32] Tom Hogan, Z. Yamani, D. Walkup, Xiang Chen, Rebecca Dally, Thomas Z. Ward, M. P. M. Dean, John Hill, Z. Islam, Vidya Madhavan, and Stephen D. Wilson, *Phys. Rev. Lett.* **114**, 257203 (2015).
- [33] A. de la Torre, E. C. Hunter, A. Subedi, S. McKeown Walker, A. Tamai, T. K. Kim, M. Hoesch, R. S. Perry, A. Georges, and F. Baumberger, *Phys. Rev. Lett.* **113**, 256402 (2014).
- [34] J. He, H. Hafiz, T. R. Mion, T. Hogan, C. Dhital, X. Chen, Q. Lin, M. Hashimoto, D. H. Lu, Y. Zhang, R. S. Markiewicz, A. Bansil, S. D. Wilson, and Rui-Hua He, *Scientific Reports* **5**, 8533 (2015).
- [35] J. He, T. Hogan, T. R. Mion, H. Hafiz, Y. He, J. D. Denlinger, S.-K. Mo, C. Dhital, X. Chen, Qisen Lin, Y. Zhang, M. Hashimoto, H. Pan, D. H. Lu, M. Arita, K. Shimada, R. S. Markiewicz, Z. Wang, K. Kempa, M. J. Naughton, A. Bansil, S. D. Wilson and Rui-Hua He, *Nat. Mater.* **14**, 577 (2015).
- [36] L. J. P. Ament, M. van Veenendaal, T. P. Devereaux, J. P. Hill, and J. van den Brink, *Rev. Mod. Phys.* **83**, 705 (2011).
- [37] M. Moretti Sala, C. Henriquet, L. Simonelli, R. Verbeni, and G. Monaco, *J. Electron Spectrosc. Relat. Phenom.* **188**, 150 (2013).
- [38] Yu.V. Shvyd'ko, J.P. Hill, C.A. Burns, D.S. Coburn, B. Brajuskovic, D. Casa, K. Goetze, T. Gog, R. Khachatryan, J.-H. Kim, C.N. Kodituwakku, M. Ramanathan, T. Roberts, A. Said, H. Sinn, D. Shu, S. Stoupin, M. Upton, M. Wiczorek, H. Yavas, *Journal of Electron Spectroscopy and Related Phenomena* **188**, 140 (2013).
- [39] See supplementary materials.
- [40] C. Monney, V. Bisogni, K. Zhou, R. Kraus, V. N. Strocov, G. Behr, J. Malek, R. Kuzian, S. Drechsler, S. Johnston, A. Revcolevschi, B. Buchner, H. M. R nnow, J. van den Brink, J. Geck, and Thorsten Schmitt, *Phys. Rev. Lett.* **110**, 087403 (2013).
- [41] Y. Ding, L. Yang, C. Chen, H. Kim, M. Han, W. Luo, Z. Feng, M. Upton, D. Casa, Jung-ho Kim, T. Gog, Z. Zeng, G. Cao, H. Mao, and M. van Veenendaal, *Phys. Rev. Lett.* **116**, 216402 (2016).
- [42] S. Bossegia, PhD Thesis, (2014), page 182, 184, 193.
- [43] M. Le Tacon, G. Ghiringhelli, J. Chaloupka, M. Moretti Sala, V. Hinkov, M. W. Haverkort, M. Minola, M. Bakr, K. J. Zhou, S. Blanco-Canosa, C. Monney, Y. T. Song, G. L. Sun, C. T. Lin, G. M. De Luca, M. Salluzzo, G. Khaliullin, T. Schmitt, L. Braicovich and B. Keimer, *Nature Physics* **7**, 725 (2011).
- [44] M. P. M. Dean, G. Dellea, R. S. Springell, F. Yakhou-Harris, K. Kummer, N. B. Brookes, X. Liu, Y.-J. Sun, J. Strle, T. Schmitt, L. Braicovich, G. Ghiringhelli, I. Bozovic, and J. P. Hill, *Nature Materials* **12**, 1019 (2013).
- [45] Ke-Jin Zhou, Yao-Bo Huang, Claude Monney, Xi Dai, Vladimir N. Strocov, Nan-Lin Wang, Zhi-Guo Chen, Chenglin Zhang, Pengcheng Dai, Luc Patthey, Jeroen van den Brink, Hong Ding and Thorsten Schmitt, *Nature Communications* **4**, 1470 (2013).
- [46] Jonathan Pelliciari, Yaobo Huang, Tanmoy Das, Marcus Dantz, Valentina Bisogni, Paul Olalde Velasco, Vladimir N. Strocov, Lingyi Xing, Xiancheng Wang, Changqing Jin, and Thorsten Schmitt, *Phys. Rev. B* **93**, 134515 (2016).

[47] P. Dai, Rev. Mod. Phys. **87**, 855 (2015).

[48] These asymmetric dispersions could also be described by the fitting using the transverse mode of the quantum-

dimer model [30]. The fitting results are shown in the supplementary [39]. Due to the absence of the longitudinal mode at  $L = 26.5$ , it seems difficult to achieve an effective fitting using the quantum-dimer model.